RSC Advances

PAPER

View Article Online
View Journal | View Issue

Cite this: *RSC Adv.*, 2019, **9**, 5492

# Defected $ZnWO_4$-decorated $WO_3$ nanorod arrays for efficient photoelectrochemical water splitting†

Ya Cui,[ab] Lun Pan, *[ab] Ying Chen,[ab] Nisha Afzal,[a] Sana Ullah,[a] Danyang Liu,[c] Li Wang,[ab] Xiangwen Zhang[ab] and Ji-Jun Zou [ab]

Received 7th December 2018
Accepted 28th January 2019

DOI: 10.1039/c8ra10060h

rsc.li/rsc-advances

The utilization of solar energy in photoelectrochemical water splitting is a popular approach to store solar energy and minimize the dependence on fossil fuels. Herein, defected $ZnWO_4$-decorated $WO_3$ nanorod arrays with type II heterojunction structures were synthesized *via* a two-step solvothermal method. By controlling the amount of Zn precursor, $WO_3$ nanorods were decorated *in situ* with tunable amounts of $ZnWO_4$ nanoparticles. Characterization confirmed the presence of abundant $W^{5+}$ species in the defected $ZnWO_4$-decorated $WO_3$ samples, leading to enhanced light absorption and charge-separation efficiency. Therefore, the decorated $WO_3$ nanorod arrays show much higher photoelectrochemical (PEC) activity than pure $WO_3$ nanorod arrays. Specifically, the sample with optimal $ZnWO_4$ decoration and surface defects exhibits a current density of 1.87 mA $cm^{-2}$ in water splitting at 1.23 V *vs.* RHE under 1 sun irradiation (almost 2.36 times higher than that of pure $WO_3$), a high incident photon-to-current efficiency of nearly 40% at 350 nm, and a relatively high photostability. However, the decoration of $WO_3$ with too much $ZnWO_4$ blocks the light absorption of $WO_3$, inhibiting the PEC performance, even when many defects are present. This work provides a promising approach to rationally construct defected heterojunctions as highly active PEC anodes for practical applications.

## 1. Introduction

As a promising method to convert solar energy into storable chemical energy, photoelectrochemical (PEC) water splitting into $H_2$ and $O_2$ has attracted wide scientific and technological interest.[1–4] Since the first discovery of PEC water splitting on $TiO_2$ by Fujishima *et al.*, many studies focused on fabricating efficient photoanodes have been conducted.[5–8] Among the various semiconductor materials, n-type tungstic oxide ($WO_3$) has emerged as a promising photoanode material for PEC water splitting because of its suitable bandgap (*ca.* 2.7 eV), which can utilize a portion of visible light, and its valence band (VB) edge (*ca.* 3 V *vs.* RHE), which is positive enough to provide a sufficient driving force for oxygen production.[9,10]

However, one of the greatest challenges hindering the photoactivity of $WO_3$ is its high rate of electron–hole recombination.[11] To solve this problem, the construction of heterostructures with matching band structures on $WO_3$ has been shown to be an efficient strategy. Type II heterojunctions, in which the both VB and conduction band (CB) of one semiconductor are either lower or higher than those of the other, are the most common composites. The formation of the proper band offset on the interface can drive photo-induced holes to the semiconductor with higher VB potential, while the electrons are driven to the semiconductor with lower CB potential. Thus, the recombination of charges is alleviated to some degree, and the spatial separation of charge carriers is enhanced.[12–16] In recent years, several semiconductors have been applied to fabricate type II heterojunctions with $WO_3$, such as $BiVO_4$,[17] BiOCl,[18] and tungstate materials (*e.g.*, $NiWO_4$,[19] $CoWO_4$,[14] and $ZnWO_4$ (ref. 20)). Among them, tungstate materials have drawn considerable attention and been widely studied due to their superior compatibility with $WO_3$ crystals. Using a modified scanning electrochemical microscope method, Leonard *et al.*[20] found that the addition of Zn to $WO_3$ resulted in the best photoperformance among 25 types of metals. Furthermore, several studies on the construction of zinc tungstate and $WO_3$ have also been carried out.[13,21,22] However, the PEC activity of $WO_3$ requires further improvement. The introduction of $W^{5+}$ species/oxygen vacancies is a promising approach because the dopant and shallow donors could prevent the recombination of photo-induced electron–hole pairs[23,24] and create defect levels below the CB, inducing new channels for light absorption and thus improving the PEC performance.[25,26]

---

[a] *Key Laboratory for Green Chemical Technology of Ministry of Education, School of Chemical Engineering and Technology, Tianjin University, Tianjin 300072, China. E-mail: panlun76@tju.edu.cn*

[b] *Collaborative Innovative Center of Chemical Science and Engineering (Tianjin), Tianjin 300072, China*

[c] *People's Public Security University of China, Beijing 100038, China*

† Electronic supplementary information (ESI) available: Lattice parameters, unit cell volumes, fitted values of $R_s$ and $R_{ct}$, XPS survey spectra of $WO_3$ and WZ-*x*, fitting of PL data for WZ-*x*, and PEC stabilities of $WO_3$ and WZ-2. See DOI: 10.1039/c8ra10060h

Herein, we develop a hydrothermal method with two steps, the formation of $WO_3$ nanorod arrays (NAs) and the reaction of Zn precursor with $WO_3$ NAs to form $ZnWO_4$ nanoparticles (NPs), to finally synthesize $ZnWO_4$-decorated $WO_3$ NAs ($WO_3/ZnWO_4$, see Scheme 1). Importantly, the insertion of Zn atoms into the $WO_3$ NA crystals leads to distortion and forms abundant $W^{5+}$ species. By controlling the amount of Zn precursor, tunable amounts of $ZnWO_4$ NPs were crystallized *in situ* on the surfaces of $WO_3$ nanorods (named WZ-*x*, where *x* reflects the content of $ZnWO_4$ NPs). Characterization confirmed the presence of abundant defects on the surface of $ZnWO_4$. Therefore, with its continuous interface, the $WO_3$/defected $ZnWO_4$ NA shows a much higher PEC activity than that of pure $WO_3$ NA. In particular, sample WZ-2 exhibits a current density as high as 1.87 mA $cm^{-2}$ in PEC water splitting at 1.23 V *vs.* RHE under 1 sun irradiation (almost 2.36 times higher than that of pure $WO_3$), a high incident photon-to-current efficiency (IPCE) of nearly 40% at 350 nm, and a relatively high photostability.

## 2. Experimental

### 2.1. Materials

Ammonium metatungstate, $(NH_4)_6(H_2W_{12}O_{40})\cdot xH_2O$, was obtained from Innochem Chemicals. Hydrochloric acid (36–38%), $H_2O_2$ (30%), acetone and absolute ethanol were obtained from Tianjin Yuanli Chemical Institute. Zinc acetate ($Zn(CH_3COO)_2$) was obtained from J&K Scientific. All reagents were analytical grade and used without further purification. Milli-Q ultrapure water (>18 mΩ cm) was used in all experiments.

### 2.2. Sample preparation

**2.2.1 Synthesis of $WO_3$ nanorod arrays.** Glass substrates coated with fluorine-doped tin oxide (FTO) were cut into slides with dimensions of 1 cm × 5 cm and washed sequentially with acetone, absolute ethanol and deionized water for 30 min each while under ultrasonication. In a typical preparation process, 1 g of $(NH_4)_6(H_2W_{12}O_{40})\cdot xH_2O$ was dissolved in 95 mL ultrapure water followed by the addition of 3 mL hydrochloric acid (36–38%) and stirring for 5 min. Subsequently, 2 mL of $H_2O_2$ (30%) was added followed by vigorous stirring for 1 h. The as-prepared solution (20 mL) was then transferred into a Teflon-lined autoclave (50 mL) in which the FTO substrate had been placed at an angle against the wall of the Teflon liner with the conducting side facing down. Hydrothermal synthesis was conducted at 160 °C for 4 h. The resulting $WO_3$ NA/FTO was rinsed with ultrapure water and dried at 60 °C for 12 h. Finally, the obtained sample was annealed at 500 °C in air for 1 h at a heating rate of 5 °C $min^{-1}$.

**2.2.2 Synthesis of $WO_3$/defected $ZnWO_4$ nanorod arrays (NAs).** $WO_3$/defected $ZnWO_4$ NAs were synthesized from the above $WO_3$ NA/FTO *via* a hydrothermal growth process using only Zn precursor. Briefly, $WO_3$ NA/FTO was added to a solution of 20 mL ethanol containing zinc acetate at a concentration of $c_x$ mM ($c_1$, $c_2$, $c_3$). The solution was then solvothermally treated in a Teflon-lined autoclave at 180 °C for 24 h. Subsequently, the obtained film was washed with absolute ethanol, dried at 60 °C overnight, and annealed at 500 °C in air for 1 h (at a heating rate of 5 °C $min^{-1}$). The molar concentration of $Zn(CH_3COO)_2$ in the prepared solution was fixed as $c_1 = 3.125$ mM, $c_2 = 6.25$ mM or $c_3 = 12.5$ mM, and the obtained films were named WZ-*x* (WZ-1, WZ-2, or WZ-3, respectively).

### 2.3. Characterization

Crystal structures were characterized by X-ray diffraction (XRD) using a Rigaku D/MAX-2500 diffractometer equipped with Cu Kα radiation at 40 kV and 140 mA at a scanning rate of 5° $min^{-1}$. Raman spectra were obtained using a Raman spectrometer (DXR Microscope) with a green semiconductor laser (532 nm) as the excitation source. Scanning electron microscopy (SEM) images were recorded using a field-emission scanning electron microscope (Hitachi, S-4800). High-resolution transmission electron microscopy (TEM) observations were made with a Tecnai $G^2$ F-20 transmission electron microscope. X-ray spectroscopy (EDX) elemental maps were obtained using an EDX system attached to the TEM instrument. X-ray photoelectron spectroscopy (XPS) was carried out using a PHI-1600 X-ray photoelectron spectroscope equipped with Al Kα radiation. The binding energy was calibrated by the C1s peak (284.8 eV). Ultraviolet-visible (UV-Vis) diffuse reflectance spectroscopy (DRS) was conducted with a Shimadzu UV-2600 spectrometer equipped with a 60 mm-diameter integrating sphere using $BaSO_4$ as the reflectance. Steady-state photoluminescence (PL) spectra were recorded using a Hitachi F-4600 instrument with excitation at 325 nm.

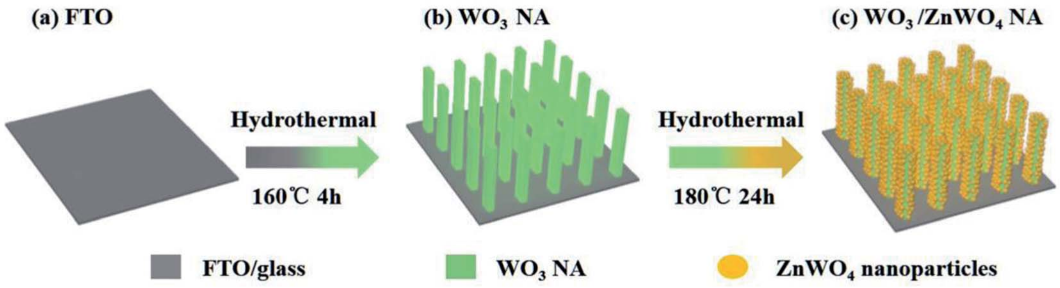

Scheme 1 Synthetic process of $WO_3$/defected $ZnWO_4$ nanorod arrays (NAs).

### 2.4. Measurement of photoanode PEC performance

The PEC properties of the as-prepared WZ-*x* samples were evaluated in a typical three-electrode quartz cell with a Pt wire counter electrode and a saturated Ag/AgCl reference electrode in 0.5 M $Na_2SO_4$ electrolyte. The illumination source was a 300 W Xe arc lamp (100 mW $cm^{-2}$, PLS-SXE300, Beijing Trusttech. Co. Ltd). Linear sweep voltammetry (LSV) was conducted by sweeping the potential to the positive direction at a scan rate of 10 mV $s^{-1}$. Based on the Nernst equation, $E$ (*vs.* RHE) = $E$ (*vs.* Ag/AgCl) + 0.059 × pH + 0.197,[27] the potential *vs.* Ag/AgCl reference electrode was converted to the potential *vs.* RHE.

The PEC stability (*I*–*t* curve) was evaluated at a potential of 0.4 V *vs.* Ag/AgCl under AM 1.5 G simulated sunlight irradiation. Electrochemical impedance spectroscopy (EIS) measurements were recorded with a sinusoidal ac perturbation of 10 mV applied over the frequency range of 1–$10^5$ Hz.

The IPCE was calculated according to eqn (1):[28]

$$\text{IPCE}\ (\lambda) = (1240 \times I)/(\lambda \times J_{\text{light}}) \times 100\%, \qquad (1)$$

where $\lambda$ is the wavelength (nm), $I$ is the photocurrent density (mA $cm^{-2}$), and $J_{\text{light}}$ is the incident power illumination density of monochromatic light (mW $cm^{-2}$).

Supposing 100% faradaic efficiency, the applied bias photon-to-current efficiency (ABPE) was calculated by eqn (2):[2]

$$\text{ABPE} = I \times (1.23 - V_{\text{bias}})/J_{\text{light}} \times 100\%, \qquad (2)$$

where $V_{\text{bias}}$ is the applied potential, and $J_{\text{light}}$ is the incident illumination power density (100 mW $cm^{-2}$).

## 3. Results and discussion

### 3.1. Crystal structure and morphology

As shown in the XRD patterns (Fig. 1a), the pure $WO_3$ NA film shows sharp and well-defined diffraction peaks corresponding to a typical monoclinic $WO_3$ phase (JCPDS no. 43-1035).[29] Compared to the pure $WO_3$ NAs, the WZ-*x* samples show new diffraction peaks at 18.87°, 30.53° and 36.28°, respectively corresponding to the (100), (111) and (021) crystal planes of pure monoclinic sanmartinite $ZnWO_4$, which has a space group of $P2/c$ with $C_{4\ 2h}$ symmetry and two molecules per unit cell ($Z = 2$; JCPDS no. 15-0774).[30] As shown in Fig. 1b, the diffraction peaks of $ZnWO_4$ were slightly shifted to higher $2\theta$ values as the content of Zn increased, resulting in smaller interplanar distances in $ZnWO_4$. This may be attributed to the existence of defects formed during the synthetic process with the insertion/substitution of Zn atoms on the surface of $WO_3$. The results in Table S1 (ESI†) indicate slight variations in the lattice parameters and cell volumes of $ZnWO_4$ (compared with JCPDS card no. 15-0774). This suggests the distortion of the octahedral $[ZnO_6]$ and $[WO_6]$ clusters, generating crystal defects in the $ZnWO_4$ lattice.[31]

The crystal structures of the as-prepared photoanodes were also verified by Raman spectroscopy (Fig. 1c). Pure $WO_3$ exhibits six main Raman peaks located at *ca.* 74, 136, 274, 328, 718 and 808 $cm^{-1}$, which are attributed to the active Raman scattering modes of monoclinic $WO_3$.[23,32] The strong Raman peaks at 718 and 808 $cm^{-1}$ are assigned to the W–O stretching modes, while the two other peaks at 274 and 328 $cm^{-1}$ are related to bending vibrations (W–O–W).[28] An extra peak at 906 $cm^{-1}$ is observed for WZ-*x* samples and can be ascribed to symmetric stretching ($\leftarrow O \leftarrow W \rightarrow O \rightarrow$), which is contributed to by the newly generated $ZnWO_4$ crystals.[33] The intensity of the peak at 906 $cm^{-1}$ increases gradually with increasing Zn amount (from WZ-1 to WZ-3). Furthermore, the synthesized crystals exhibit a relatively broad vibrational mode, indicating short-range structural disorder.[34]

The surface morphologies of the WZ-*x* samples were characterized by SEM and TEM, as shown in Fig. 2. $WO_3$ exhibits a uniform rod-like morphology. The rods are cuboid shaped with lengths of 500 nm to 1.5 μm, widths of 200–400 nm, and heights of *ca.* 2.4 μm (Fig. 2a and b). After secondary solvothermal crystallization and thermal calcination (WZ-*x* samples), the surface layers of the $WO_3$ arrays are converted to $ZnWO_4$ NPs, forming a well-contacted heterojunction structure (Fig. 2c–h). Compared to the pristine $WO_3$ NAs, the WZ-*x* samples show much rougher surfaces after the formation of $ZnWO_4$ NP layers. Compared to the other WZ-*x* samples, the lowest concentration of Zn precursor (3.125 mM; WZ-1) resulted in relatively fewer $ZnWO_4$ NPs with crystal sizes of *ca.* 20–40 nm. When the Zn precursor concentration was increased to 6.25 mM (WZ-2), the amount of $ZnWO_4$ NPs increased along with the crystal size (*ca.* 50 nm). Further increasing the concentration of

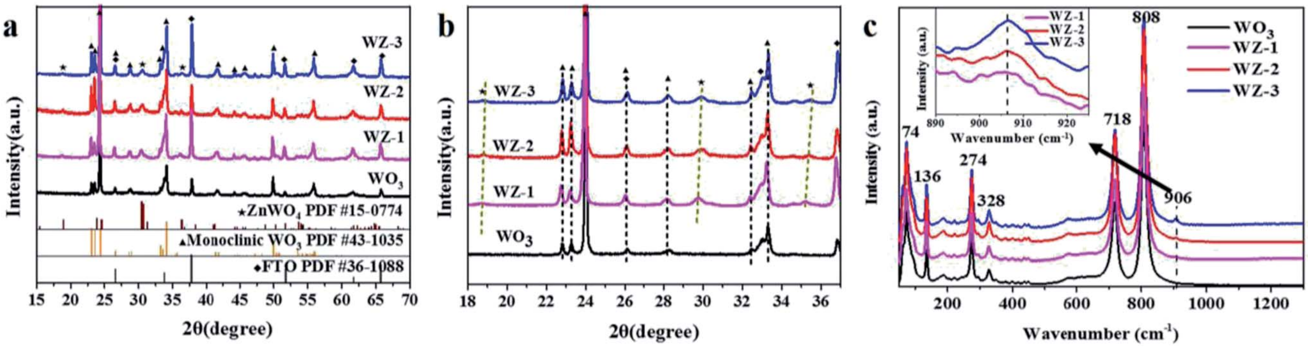

Fig. 1 XRD patterns (a and b) and Raman spectra (c) of pure $WO_3$ and WZ-*x* NAs.

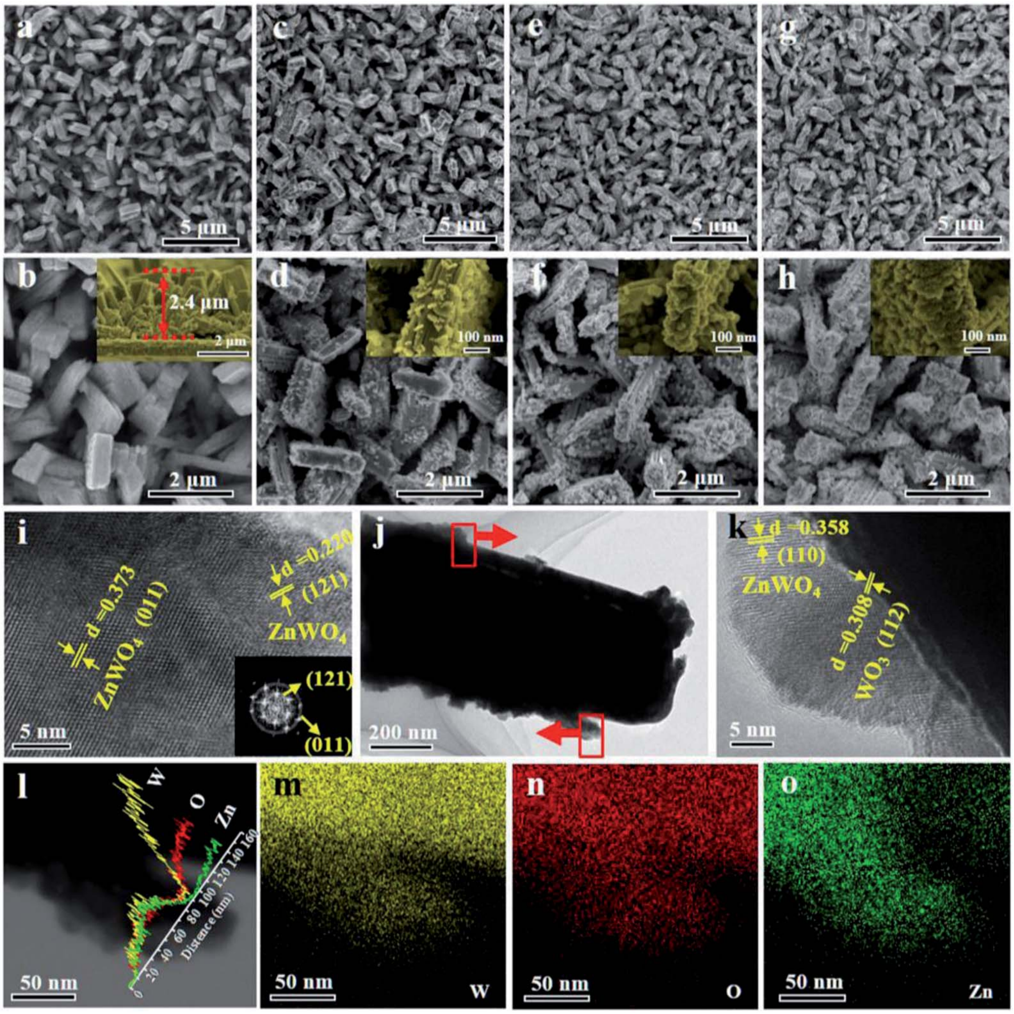

Fig. 2 SEM images of $WO_3$ (a and b), WZ-1 (c and d), WZ-2 (e and f) and WZ-3 (g and h). TEM images (i–k) and EDX element line scans (l) and maps (m–o) of WZ-2. The inset in (b) is the cross-sectional view of a $WO_3$ NA.

Zn precursor to 12.5 mM (WZ-3) caused the $ZnWO_4$ NPs to become much larger and denser, almost covering the surface of $WO_3$ completely. This dense coverage might inhibit optical absorption and mass transfer for the PEC reaction.

The moderate coverage of $ZnWO_4$ on $WO_3$ in sample WZ-2 should promote optical absorption and facilitate the separation of generated electron–hole pairs for the constructed heterojunction. Moreover, this hierarchically structured film can provide sufficient surface active sites to effectively enable reactions at the interface between the photoanode and electrolyte, thus improving the PEC performance.[35]

The TEM images (Fig. 2i–k) confirm the formation of $WO_3$/$ZnWO_4$ NAs. The spacing of 0.308 nm is in good agreement with the interplanar spacing of the $WO_3$ (112) plane,[36] while the spacings of 0.358, 0.373 and 0.220 nm can be indexed to the (110), (011) and (121) planes of monoclinic $ZnWO_4$.[37] The corresponding fast Fourier transform (FFT) pattern (inset in Fig. 2i) clearly reveals that the $ZnWO_4$ NPs are highly crystalline. It is worth noting that an compact interface in the $WO_3$/$ZnWO_4$ heterojunction was formed (Fig. 2k). This can be attributed to the *in situ* reaction of the Zn precursor with $WO_3$ NAs, which is beneficial for the migration of photogenerated carriers between the two composites. Meanwhile, the elemental line scanning profiles (Fig. 2l) confirm that W and O are dispersed in the nanorods and branched $ZnWO_4$ regions, while Zn exists only in the surrounding $ZnWO_4$ regions. This further verifies that $WO_3$ was decorated with well-defined defected $ZnWO_4$ in sample WZ-2. Similarly, the EDX maps (Fig. 2m–o) also confirm the primary distribution of W (and O) and Zn in the rod core and on the surface, respectively.[11,38]

### 3.2. Chemical state

XPS was conducted to detect the surface chemical states of the as-prepared photoanodes. The survey spectra (Fig. S1a, ESI†) show the presence of W, O and Zn in the pure $WO_3$ and WZ-*x* samples without any impurities. In the high-resolution O 1s XPS spectra (Fig. S1b, ESI†), the peak with a binding energy of 530.5 eV is attributed to O–W and O–Zn bonds.[39,40] The Zn 2p XPS spectra (Fig. 3a) of the WZ-*x* samples show similar characteristic Zn $2p_{3/2}$ and Zn $2p_{1/2}$ peaks centered at 1021.9 and

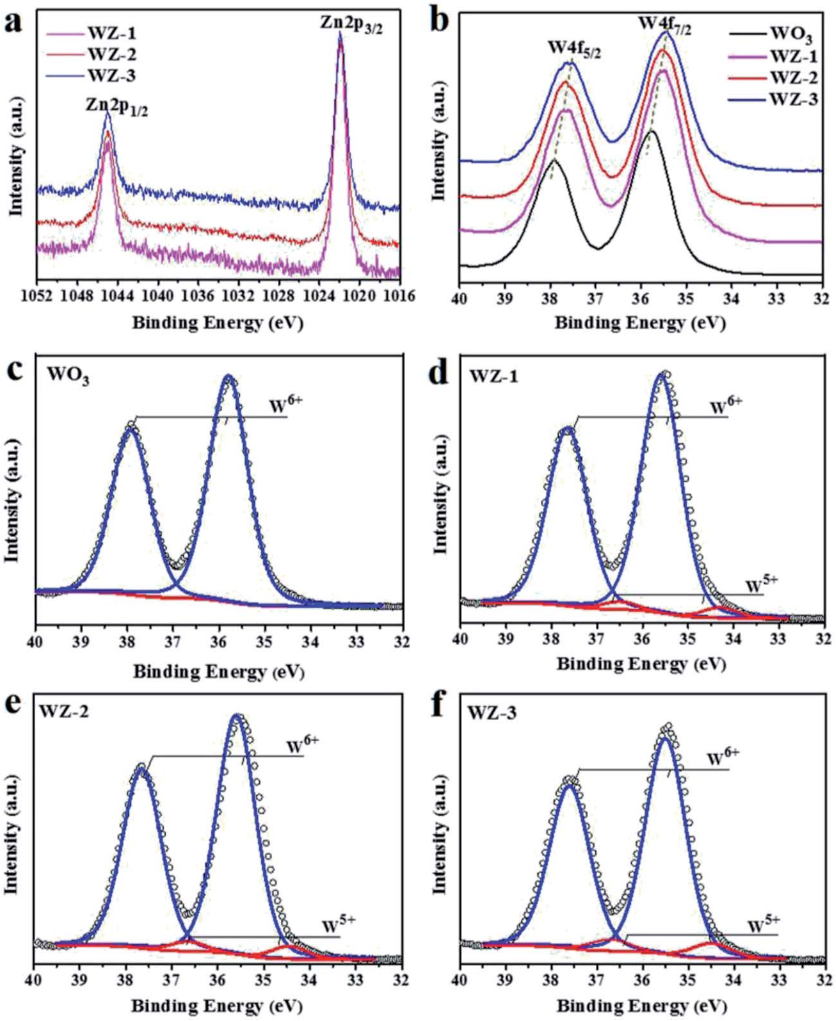

Fig. 3 XPS spectra of $WO_3$, WZ-1, WZ-2 and WZ-3: Zn2p (a) and W4f (b), and the fitted W4f XPS spectra of $WO_3$ (c), WZ-1 (d), WZ-2 (e) and WZ-3 (f).

1045.0 eV, respectively. These energies are slightly higher than those reported in the literature (1021.6 and 1044.7 eV, respectively),[40] indicating that fewer electrons locate in the Zn atoms of WZ-*x* compared to in pristine $ZnWO_4$. Because Zn has a lower electronegativity (1.65) than W (2.36), the shift in binding energy confirms the close interaction between $WO_3$ and $ZnWO_4$. As shown in Fig. 3b, the WZ-*x* samples exhibit obvious low-energy shifts in W 4f binding energy compared to pure $WO_3$. For samples WZ-2 and WZ-3, a 0.3 eV negative shift in the W 4f binding energy is observed. This indicates that the formation of WZ-*x* heterojunctions increases the outer electron cloud density of the W atom, which results from W–O–Zn bonding and/or the presence of surface defects.[41]

Pristine $WO_3$ shows only two symmetrical sharp peaks of W 4f (Fig. 3c), which is typical of $W^{6+}$, while the W 4f peak of WZ-*x* can be divided into four peaks (Fig. 3d–f). The strong peaks at 35.4 and 37.6 eV correspond to $W^{6+}$, while the weak peaks at 34.5 and 36.7 eV correspond to $W^{5+}$.[26] By fitting the XPS peak of W 4f, the contents of $W^{5+}$ in samples WZ-1, WZ-2 and WZ-3 are estimated to be 3.9%, 4.9% and 7.2% (atomic percentage), respectively, and the content of $W^{5+}$ is positively correlated with the amount of $ZnWO_4$.

### 3.3. Optical properties

The UV-Vis DRS spectra of the $WO_3$ and WZ-*x* photoanodes are shown in Fig. 4a. For pristine $WO_3$, the absorption edge appears at *ca.* 460 nm, consistent with its intrinsic band-gap absorption.[42] After coating with $ZnWO_4$ NPs, the absorption intensity is obviously enhanced in the ultraviolet region compared to pure $WO_3$. Among the WZ-*x* samples, WZ-2 achieves the best absorption due to the moderate decoration of defected $ZnWO_4$ on $WO_3$ in this sample. The enhanced optical absorption should be related to the enhanced light scattering by the rough surface. Moreover, the $W^{5+}$ species in $ZnWO_4$ create defect levels below the CB, giving rise to absorption in the far-visible and/or infrared regions and producing tailing at the onset of absorption.[21] The high-resolution VB XPS spectra of $WO_3$ and WZ-*x* were recorded to determine the VB edge. As shown in Fig. 4b, compared to pure $WO_3$ (2.8 eV),[43] the VB positions of WZ-*x* are clearly shifted toward a lower energy (0.1–0.2 eV),

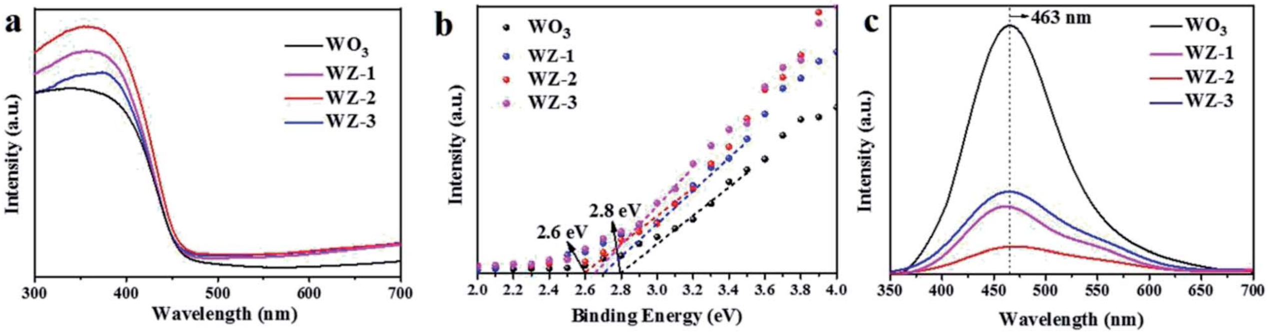

Fig. 4 UV-Vis DRS spectra (a), high-resolution VB XPS spectra (b), and photoluminescence (PL) spectra (c) of $WO_3$ and WZ-*x*.

indicating that the $ZnWO_4$ NPs have a lower VB edge (and lower CB on the basis of bandgap data[16]) than $WO_3$, which benefits the formation of type II heterojunctions.[26]

The recombination of photogenerated charge carriers was investigated through PL emission measurements. Generally, a higher PL intensity indicates a higher recombination rate of photoexcited electrons and holes, while a lower PL intensity indicates a lower recombination rate.[14] Fig. 4c shows that pure $WO_3$ and WZ-*x* exhibit a major PL emission peak centered at around 463 nm due to the intrinsic feature of $WO_3$ and/or $ZnWO_4$. This peak is ascribed to the radiative decay of self-trapped excitons in the crystals.[35,44] However, the PL intensities of WZ-*x* are clearly lower than that of pristine $WO_3$, indicating a much greater charge-separation efficiency of photoexcited electron–hole pairs. For surface $ZnWO_4$, the PL peak at *ca.* 460 nm (Fig. S2, ESI†) is mainly caused by the charge transition between the O 2p orbitals and the empty d orbitals of the central $W^{6+}$ ions in the $WO_6{}^{2-}$ complex, while the yellow-red emission is extrinsic and may be related to $W^{5+}$.[44] The defects induce the new energy states in the bandgap, which may benefit the separation efficiency of $e^-$–$h^+$ pairs.[31] Fitting the PL peak indicated that the amount of $W^{5+}$ species in WZ-*x* gradually increased with increasing Zn precursor concentration, consistent with the XPS results. However, for sample WZ-3, the total coverage of $ZnWO_4$ on the $WO_3$ surface will block light absorption and significantly inhibit the activity of $WO_3$, even when a large number of defects are present. Thus, WZ-2 with abundant defects and a heterojunction structure exhibits the highest separation efficiency of photogenerated charge carriers.[45]

### 3.4. PEC performances of photoanodes

PEC catalysis is emerging as a promising method for solar water splitting (hydrogen and oxygen generation).[9] In PEC water splitting, the oxidation and reduction processes are separated into two half-cell reactions [eqn (3) and (4)], with eqn (5) showing the overall reaction:

$$4H^+(aq) + 4e^- \rightarrow 2H_2(g),\ E^\circ = 0\ \text{V}\ \textit{vs.}\ \text{RHE} \tag{3}$$

$$2H_2O(l) \rightarrow O_2(g) + 4H^+(aq) + 4e^-,\ E^\circ = 1.23\ \text{V}\ \textit{vs.}\ \text{RHE} \tag{4}$$

$$2H_2O(l) \rightarrow O_2(g) + 2H_2(g),\ E^\circ = 1.23\ \text{V}\ \textit{vs.}\ \text{RHE} \tag{5}$$

To identify the PEC performances of the pristine $WO_3$ and WZ-*x* photoanodes, PEC measurements were performed under simulated sun light illumination (100 mW $cm^{-2}$) in 0.5 M $Na_2SO_4$ electrolyte. As shown in Fig. 5a, no current was detected for pure $WO_3$ in the dark ($WO_3$-dark). Under light illumination, the photocurrent density of pure $WO_3$ reaches 0.79 mA $cm^{-2}$ at an applied bias 1.23 V *vs.* RHE. The $ZnWO_4$-coated samples WZ-1 and WZ-3 show enhanced photocurrent densities of 1.44 and 1.24 mA $cm^{-2}$, respectively, while WZ-2 exhibits the highest photocurrent density of *ca.* 1.87 mA $cm^{-2}$ at 1.23 V *vs.* RHE, nearly 2.36 times higher than that of pure $WO_3$. The PEC performances of recently reported $WO_3$-based photoanodes are summarized in Table S2 (ESI†). Notably, WZ-2 shows a higher PEC current than the previously reported photoanodes. Moreover, the on-set potentials of the WZ-*x* photoanodes (0.70 V *vs.* RHE for WZ-1, 0.68 V for WZ-2, and 0.75 V for WZ-3) are also lower than that of pure $WO_3$ (0.77 V *vs.* RHE). Based on the LSV results in Fig. 5a, WZ-2 achieved the maximum ABPE in this study (0.18% at 1.05 V *vs.* RHE; Fig. 5b), compared to only 0.07% for pure $WO_3$.

The IPCE for PEC water splitting was carried out at 1.2 V *vs.* RHE, and the results are shown in Fig. 5c. The wavelengths of the initial light response are below 470 nm for the pure $WO_3$ and WZ-*x* photoanodes and IPCE increases gradually as the irradiation wavelength decreases. Based on the IPCE values, the PEC decreases in the following order: WZ-2 > WZ-1 > WZ-3 > pure $WO_3$. The IPCE value of WZ-2 reaches 40% at 350 nm. Sample WZ-2 also possesses relatively good photostability, with only a slight loss after long-term continuous illumination (Fig. S3, ESI†). After continuous PEC testing (over 3 h), WZ-2 shows nearly the same XRD peaks (Fig. S4a, ESI†) and surface morphology (Fig. S4b, ESI†) as those of a fresh sample, again confirming the relatively good photostability of WZ-2.

For the $WO_3$ photoanode, the occurrence of hole-capture reactions (*e.g.*, $2H_2O + 2h^+ \rightarrow H_2O_2 + 2H^+$) on the surface is responsible for the corrosion of $WO_3$ *via* the formation of peroxotungstates, which hinders charge transfer at the $WO_3$/electrolyte interface. In WZ-*x* samples, the decoration of $WO_3$ with defected $ZnWO_4$ forms a type II heterogeneous structure. Since $ZnWO_4$ possesses higher VB positions than $WO_3$, the photoinduced holes will transfer rapidly to the $ZnWO_4$ NPs, preventing the accumulation of holes on $WO_3$ and preventing the photocorrosion of $WO_3$. In addition, $ZnWO_4$ has better

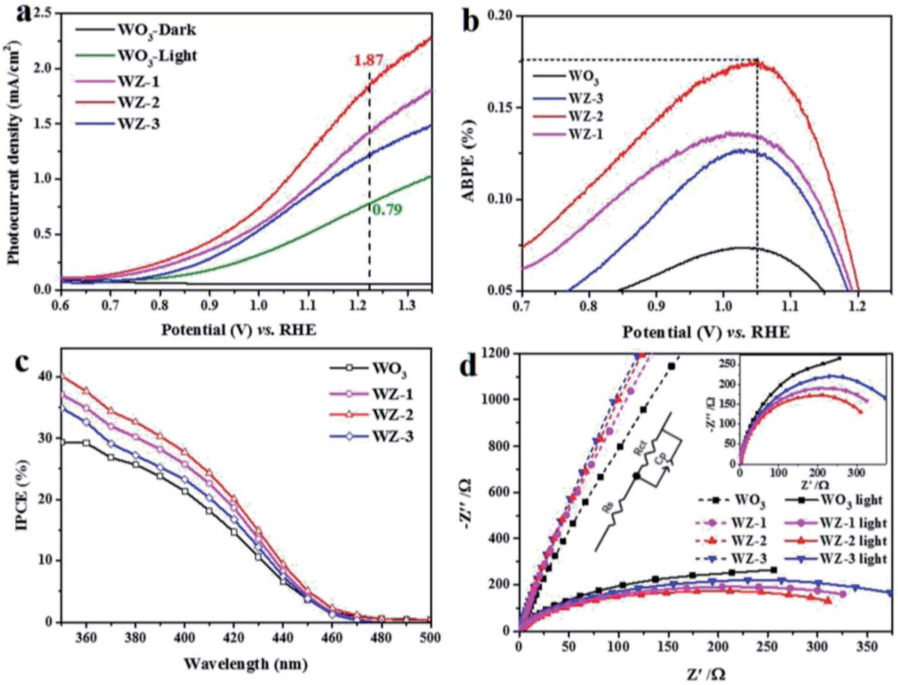

Fig. 5 PEC properties of $WO_3$ and WZ-*x* photoanodes in a 0.5 M $Na_2SO_4$ aqueous solution at pH = 6.8 under light illumination (100 mW $cm^{-2}$). *J*–*V* curves (a), applied bias photon-to-current efficiency (ABPE) (b), incident photon to current efficiency (IPCE) at 1.2 V *vs.* RHE (c), and electrochemical impedance spectroscopy (EIS) spectra recorded in the dark and under light irradiation (d). The inset in (d) shows the EIS fitting model. $R_s$, series resistance; $R_{ct}$, charge-transfer resistance; $C_p$, capacitive reactance.

chemical stability and photocorrosion resistance than $WO_3$.[20,31] Therefore, the decoration of $WO_3$ with $ZnWO_4$ benefits the stability of the photoanode.

To obtain more insight into the charge-transfer kinetics of the photoanodes, EIS measurements were carried out. The arc radii of the Nyquist plots can be used to evaluate the charge-transfer resistance at the semiconductor/electrolyte interface, with a smaller arc radius implying a smaller charge-transfer resistance.[46] Based on the EIS plots (Fig. 5d), the light irradiation significantly decreases the arc radius of the photoanode, and the effect is more obvious for WZ-*x* than for pure $WO_3$. This suggests that WZ-*x* exhibits more efficient light absorption and conversion than pure $WO_3$. The charge-transfer resistances of the photoanodes were calculated by fitting the EIS spectra (see the inset in Fig. 5d), where $R_s$ and $R_{ct}$ represent the series resistance and interfacial charge-transfer resistance across the electrode/electrolyte interface, respectively.[47] The fitted values of each component are listed in Table S3 (ESI†). The $R_s$ values for all photoanodes are similar, indicating that the series resistance effect is negligible. In the dark, $R_{ct}$ decreases as the amount of $ZnWO_4$ NPs decreases ($R_{ct}$ = 35 552 Ω for WZ-3, 34 638 Ω for WZ-2, 33 858 Ω for WZ-1, and 31 347 Ω for pure $WO_3$). However, under light irradiation, the $R_{ct}$ values of all of the photoanodes are obviously decreased, and the order is also altered ($R_{ct}$ = 592 Ω for $WO_3$, 488.5 Ω for WZ-3, 422.4 Ω for WZ-1, and 391.3 Ω for WZ-2, consistent with the PEC performances of the photoanodes). Notably, the construction of WZ-*x* heterojunctions benefits charge transfer under light irradiation, unless the coating of defected $ZnWO_4$ is too thick (WZ-3).

Scheme 2 shows the proposed process of charge separation and transfer for $WO_3$/defected $ZnWO_4$ NAs. As reported, the CB and VB energies of $WO_3$ are 0.64 and 3.3 V, respectively, while the corresponding values for $ZnWO_4$ are −0.1 and 3.05 V, respectively.[13,20] As the shallow donors, the surface $W^{5+}$ species in $ZnWO_4$ will introduce a new band level below the CB (*ca.* 0.30 V, calculated based on the peak emission wavelength in the PL spectrum). Therefore, the matched band structures benefit the formation of interface heterojunctions between $WO_3$ and defected $ZnWO_4$ in the WZ-*x* samples. Under light illumination, the electrons are excited from the VBs of $WO_3$ and $ZnWO_4$ to their own CBs, leaving positive holes in the VBs. The photogenerated electrons in the CB of the $ZnWO_4$ NPs would first

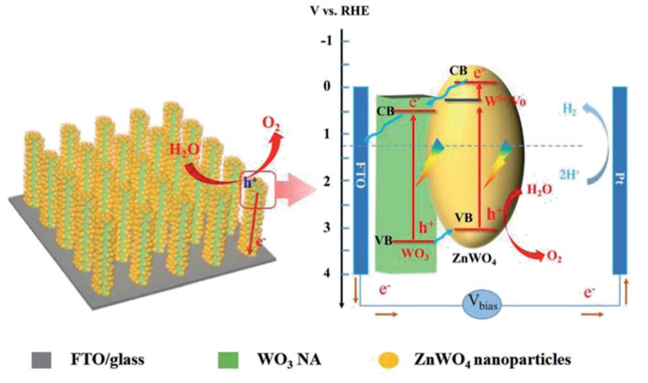

Scheme 2 Schematic diagram of the $WO_3$@defected $ZnWO_4$ photoanode and the proposed charge-transfer processes.

migrate to the band of $W^{5+}$ (or related oxygen vacancies) and then to the CB of $WO_3$. The accumulated electrons will rapidly transfer from $WO_3$ to the FTO substrate *via* back contact and finally reach the Pt counter electrode for hydrogen generation. Meanwhile, the photogenerated holes in the VB of $WO_3$ have a higher probability of transferring to the surface of $ZnWO_4$ because of the internal electric field of the heterojunction. Thus, the holes have a higher probability of reacting with water molecules to generate oxygen gas.

The good PEC performance of sample WZ-2 in this study should be closely related to the heterojunction and surface $W^{5+}$ species. The heterojunction will force the spatial separation of electrons and holes in $WO_3$ and $ZnWO_4$, respectively, while the surface $W^{5+}$ species will inhibit charge recombination.

## 4. Conclusions

Using a two-step solvothermal method, we successfully fabricated $WO_3$/defected $ZnWO_4$ as a photoanode for efficient PEC water splitting. By controlling the amount of Zn precursor, tunable amounts of $ZnWO_4$ nanoparticles were decorated on $WO_3$ nanorods. The type II heterojunction with abundant defects enhances the light absorption and charge-separation efficiency. Thus, the WZ-*x* samples show much higher PEC activities than those of pure $WO_3$ NA. Among the samples, WZ-2 exhibits the highest photocurrent, with a current density of 1.87 mA $cm^{-2}$ in PEC water splitting at 1.23 V *vs.* RHE (almost 2.36 times higher than that of pure $WO_3$), a high IPCE of *ca.* 40% at 350 nm, and a relatively high photostability. This work paves the way for fabricating highly active PEC anodes with defected heterojunction structures for practical applications.

## Conflicts of interest

There are no conflicts to declare.

## Acknowledgements

The authors appreciate the support from the National Natural Science Foundation of China (21506156, 21676193, 51661145026) and the Tianjin Municipal Natural Science Foundation (16JCQNJC05200, 15JCZDJC37300).

## Notes and references

1 S. Ye, C. Ding, R. Chen, F. Fan, P. Fu, H. Yin, X. Wang, Z. Wang, P. Du and C. Li, *J. Am. Chem. Soc.*, 2018, **140**, 3250–3256.

2 Y. Bi, B. Zhang, L. Wang, Y. Zhang and Y. Ding, *Angew. Chem., Int. Ed.*, 2018, **57**, 2248–2252.

3 L. Pan, S. Wang, J. Xie, L. Wang, X. Zhang and J.-J. Zou, *Nano Energy*, 2016, **28**, 296–303.

4 X.-T. Xu, L. Pan, X. Zhang, L. Wang and J.-J. Zou, *Adv. Sci.*, 2019, **6**, 1801505.

5 A. Fujishima and K. Honda, *Nature*, 1972, **238**, 37–38.

6 L. Pan, T. Muhammad, L. Ma, Z.-F. Huang, S. Wang, L. Wang, J.-J. Zou and X. Zhang, *Appl. Catal., B*, 2016, **189**, 181–191.

7 S. Wang, X. Zhang, S. Li, Y. Fang, L. Pan and J.-J. Zou, *J. Hazard. Mater.*, 2017, **331**, 235–245.

8 D. K. Lee and K.-S. Choi, *Nat. Energy*, 2018, **3**, 53–60.

9 J. Huang, Y. Zhang and Y. Ding, *ACS Catal.*, 2017, **7**, 1841–1845.

10 N. Zhang, X. Li, H. Ye, S. Chen, H. Ju, D. Liu, Y. Lin, W. Ye, C. Wang, Q. Xu, J. Zhu, L. Song, J. Jiang and Y. Xiong, *J. Am. Chem. Soc.*, 2016, **138**, 8928–8935.

11 P. M. Rao, L. Cai, C. Liu, I. S. Cho, C. H. Lee, J. M. Weisse, P. Yang and X. Zheng, *Nano Lett.*, 2014, **14**, 1099–1105.

12 Y. Hou, F. Zuo, A. P. Dagg, J. K. Liu and P. Y. Feng, *Adv. Mater.*, 2014, **26**, 5043–5049.

13 K. Yuan, Q. Cao, X. Li, H.-Y. Chen, Y. Deng, Y.-Y. Wang, W. Luo, H.-L. Lu and D. W. Zhang, *Nano Energy*, 2017, **41**, 543–551.

14 H. Zhang, W. Tian, Y. Li, H. Sun, M. O. Tade and S. Wang, *J. Mater. Chem. A*, 2018, **6**, 6265–6272.

15 S. Cao, X. Yan, Z. Kang, Q. Liang, X. Liao and Y. Zhang, *Nano Energy*, 2016, **24**, 25–31.

16 X. Cheng, S. Cao, Y. Huan, Z. Bai, M. Li, H. Wu, R. Zhang, W. Peng, Z. Ji and X. Yan, *Energy Technol.*, 2018, DOI: 10.1002/ente.201800899.

17 J. H. Baek, B. J. Kim, G. S. Han, S. W. Hwang, D. R. Kim, I. S. Cho and H. S. Jung, *ACS Appl. Mater. Interfaces*, 2017, **9**, 1479–1487.

18 W. Yang, Y. Wen, D. Zeng, Q. Wang, R. Chen, W. Wang and B. Shan, *J. Mater. Chem. A*, 2014, **2**, 20770–20775.

19 S. F. Anis, B. S. Lalia, G. Palmisano and R. Hashaikeh, *J. Mater. Sci.*, 2017, **53**, 2208–2220.

20 K. C. Leonard, K. M. Nam, H. C. Lee, S. H. Kang, H. S. Park and A. J. Bard, *J. Phys. Chem. C*, 2013, **117**, 15901–15910.

21 Y. Keereeta, S. Thongtem and T. Thongtem, *Powder Technol.*, 2015, **284**, 85–94.

22 Y. Keereeta, T. Thongtem and S. Thongtem, *J. Alloys Compd.*, 2011, **509**, 6689–6695.

23 G. M. Wang, Y. C. Ling, H. Y. Wang, X. Y. Yang, C. C. Wang, J. Z. Zhang and Y. Li, *Energy Environ. Sci.*, 2012, **5**, 6180–6187.

24 P. Chen, M. Baldwin and P. R. Bandaru, *J. Mater. Chem. A*, 2017, **5**, 14898–14905.

25 A. Naldoni, M. Allieta, S. Santangelo, M. Marelli, F. Fabbri, S. Cappelli, C. L. Bianchi, R. Psaro and V. Dal Santo, *J. Am. Chem. Soc.*, 2012, **134**, 7600–7603.

26 X. Jia, M. Tahir, L. Pan, Z.-F. Huang, X. Zhang, L. Wang and J.-J. Zou, *Appl. Catal., B*, 2016, **198**, 154–161.

27 X. Chang, T. Wang, P. Zhang, J. Zhang, A. Li and J. Gong, *J. Am. Chem. Soc.*, 2015, **137**, 8356–8359.

28 H. Zhang, W. Zhou, Y. Yang and C. Cheng, *Small*, 2017, **13**, 1603840.

29 J. Zhang, X. Chang, C. Li, A. Li, S. Liu, T. Wang and J. Gong, *J. Mater. Chem. A*, 2017, **6**, 3267–3756.

30 Y. Huang, Y. Gao, Q. Zhang, J.-j. Cao, R.-j. Huang, W. Ho and S. C. Lee, *Appl. Catal., A*, 2016, **515**, 170–178.

31 P. F. S. Pereira, A. F. Gouveia, M. Assis, R. C. de Oliveira, I. M. Pinatti, M. Penha, R. F. Gonçalves, L. Gracia,

J. Andrés and E. Longo, *Phys. Chem. Chem. Phys.*, 2018, **20**, 1923–1937.

32 N. Datta, N. Ramgir, M. Kaur, M. Roy, R. Bhatt, S. Kailasaganapathi, A. K. Debnath, D. K. Aswal and S. K. Gupta, *Mater. Chem. Phys.*, 2012, **134**, 851–857.

33 D. Errandonea, F. J. Manjón, N. Garro, P. Rodríguez-Hernández, S. Radescu, A. Mujica, A. Muñoz and C. Y. Tu, *Phys. Rev. B: Condens. Matter Mater. Phys.*, 2008, **78**, 054116.

34 E. Longo, D. P. Volanti, V. M. Longo, L. Gracia, I. C. Nogueira, M. A. P. Almeida, A. N. Pinheiro, M. M. Ferrer, L. S. Cavalcante and J. Andrés, *J. Phys. Chem. C*, 2014, **118**, 1229–1239.

35 X. Fan, B. Gao, T. Wang, X. Huang, H. Gong, H. Xue, H. Guo, L. Song, W. Xia and J. He, *Appl. Catal., A*, 2016, **528**, 52–58.

36 L. Santos, P. Wojcik, J. V. Pinto, E. Elangovan, J. Viegas, L. Pereira, R. Martins and E. Fortunato, *Adv. Electron. Mater.*, 2015, **1**, 1400002.

37 S. Huang, Y. Feng, L. Han, W. Fan, X. Zhao, Z. Lou, Z. Qi, B. Yu and N. Zhu, *RSC Adv.*, 2014, **4**, 61679–61686.

38 X. Shi, I. Y. Choi, K. Zhang, J. Kwon, D. Y. Kim, J. K. Lee, S. H. Oh, J. K. Kim and J. H. Park, *Nat. Commun.*, 2014, **5**, 4775.

39 B. Jin, E. Jung, M. Ma, S. Kim, K. Zhang, J. I. Kim, Y. Son and J. H. Park, *J. Mater. Chem. A*, 2018, **6**, 2585–2592.

40 J. Lu, M. Liu, S. Zhou, X. Zhou and Y. Yang, *Dyes Pigm.*, 2017, **136**, 1–7.

41 S. S. Kalanur, I.-H. Yoo, K. Eom and H. Seo, *J. Catal.*, 2018, **357**, 127–137.

42 Y. Liu, C. Xie, H. Li, H. Chen, T. Zou and D. Zeng, *J. Hazard. Mater.*, 2011, **196**, 52–58.

43 M. Ma, K. Zhang, P. Li, M. S. Jung, M. J. Jeong and J. H. Park, *Angew. Chem., Int. Ed.*, 2016, **55**, 11819–11823.

44 P. Siriwong, T. Thongtem, A. Phuruangrat and S. Thongtem, *CrystEngComm*, 2011, **13**, 1564–1569.

45 W. He, R. Wang, L. Zhang, J. Zhu, X. Xiang and F. Li, *J. Mater. Chem. A*, 2015, **3**, 17977–17982.

46 S. Wang, L. Pan, J.-J. Song, W. Mi, J.-J. Zou, L. Wang and X. Zhang, *J. Am. Chem. Soc.*, 2015, **137**, 2975–2983.

47 A. Thapa, J. Zai, H. Elbohy, P. Poudel, N. Adhikari, X. Qian and Q. Qiao, *Nano Res.*, 2014, **7**, 1154–1163.